Chapter 2
Hierarchically Nanostructured Photoelectrodes for Quantum-Dot-Sensitized Solar Cells

Eui-Hyun Kong, Yong-June Chang, and Hyun Myung Jang

Abstract Quantum-dot-sensitized solar cells (QDSSCs) recently have attracted a great deal of attention owing to their advantages that include high molar extinction coefficient of quantum dots, tunable energy gaps, and multiple exciton generation. However, various architectures have not yet been proposed as alternative working electrodes for QDSSCs. In this article, two hierarchical nanostructures will be presented as next-generation photoelectrodes for highly-efficient QDSSCs: (a) the tertiary-hierarchically-structured mesoporous spherical (MS) TiO_2 and (b) the sea urchin TiO_2 (SU TiO_2) particles composed of radially aligned rutile TiO_2 nanowires. The MS TiO_2 offers a high surface area, a high internal reflectance in the visible region, and good pore accessibility. A conversion efficiency of 1.9 % was achieved by CdS QDSSCs made with the MS TiO_2 photoelectrode, which corresponds to ~58 % improvement as compared with the values obtained from the conventional devices made with 20-nm-sized nanocrystalline TiO_2 film. Secondly, SU TiO_2 was incorporated into the TiO_2 nanoparticle (NP) network to construct the SU–NP composite film and applied to the CdS/CdSe/ZnS QDSSCs. A conversion efficiency of 4.2 % was achieved, which corresponds to ~20 % improvement as compared with the values obtained from the reference cell made of the NP film. We attribute this extraordinary result to the light scattering effect and efficient charge collection. Thus, the SU TiO_2 and MS TiO_2 can be promising materials for the photoanodes of QDSSCs.

Z.M. Wang, A. Neogi (eds.), *Nanoscale Photonics and Optoelectronics*, Lecture Notes in Nanoscale Science and Technology 9, DOI 10.1007/978-1-4419-7587-4_2,

E.-H. Kong • Y.-J. Chang • H.M. Jang (✉)
Department of Materials Science and Engineering, and Division of Advanced Materials Science, Pohang University of Science and Technology (POSTECH), Pohang 790-784, Republic of Korea
e-mail: hmjang@postech.ac.kr

J. Wu and Z.M. Wang (eds.), *Quantum Dot Solar Cells*, Lecture Notes in Nanoscale Science and Technology 15, DOI 10.1007/978-1-4614-8148-5_2,

2.1 Introduction

Dye-sensitized solar cells (DSSCs) consisting of a wide band-gap semiconductor film, a dye, and an electrolyte have been regarded as a promising alternative to silicon-based photovoltaic cells [1]. Instead of using a dye, the sensitization of a photoanode can be achieved through modification of the oxide surface with a narrow band-gap semiconductor quantum-dot (QD). Quantum-dot-sensitized solar cells (QDSSCs) recently have attracted a great deal of attention owing to their advantages over DSSCs. The advantages include (a) higher molar extinction coefficient [2] of QDs than ruthenium complexes [3, 4], (b) tunable energy gaps [5], and (c) multiple exciton generation (MEG) [6] which may potentially lead to a theoretical maximum efficiency [7] higher than that of DSSCs.

Recently, hierarchically structured oxide materials such as ZnO aggregates [8], nano-embossed hollow spherical TiO_2 [9], and mesoporous TiO_2 beads [10–12] have been reported as functional photoelectrode materials in the sensitized photovoltaic devices. These porous spherical systems consist of nano-sized crystallites that are aggregated to create micrometer- or submicrometer-sized secondary particles and thereby can function as light scattering materials with maintaining a large internal surface area for sufficient sensitizer-uptake. Thus, these bi-functional materials having 0–3 hierarchy seem to be more appealing than traditional nanocrystalline TiO_2. However, slow-trap-limited electron transport remains a problem in the charge collection kinetics.

Herein, we will introduce two hierarchical nanostructures: tertiary hierarchically structured TiO_2 and sea urchin TiO_2.

2.2 Theoretical Backgrounds

2.2.1 Quantum Confinement Effect

Quantum dots are semiconductor nanocrystals that have unique optical properties because of a combination of their band-gap energy and quantum-well phenomena. The dots of a few nanometers behave similarly to three-dimensional quantum wells. When an electron in the quantum dot is excited by a photon, it behaves as a particle confined in an infinite potential well. In the quantum dot, the density of states is discrete, and the band gap is determined by the size of the quantum dot. Through the theoretical calculations, the size dependence is plotted as a function of the inverse radius squared in Fig. 2.1a [13]. The experimental result also confirms that the absorption curves become blue-shifted with decreasing particle size as demonstrated in Fig. 2.1b [14].

In quantum mechanics, a proper approach to the behavior of an exciton is the 3-D model of a particle in a box [15] because the behavior of a particle is fundamentally described by the wavefunction Ψ which is the solution of the

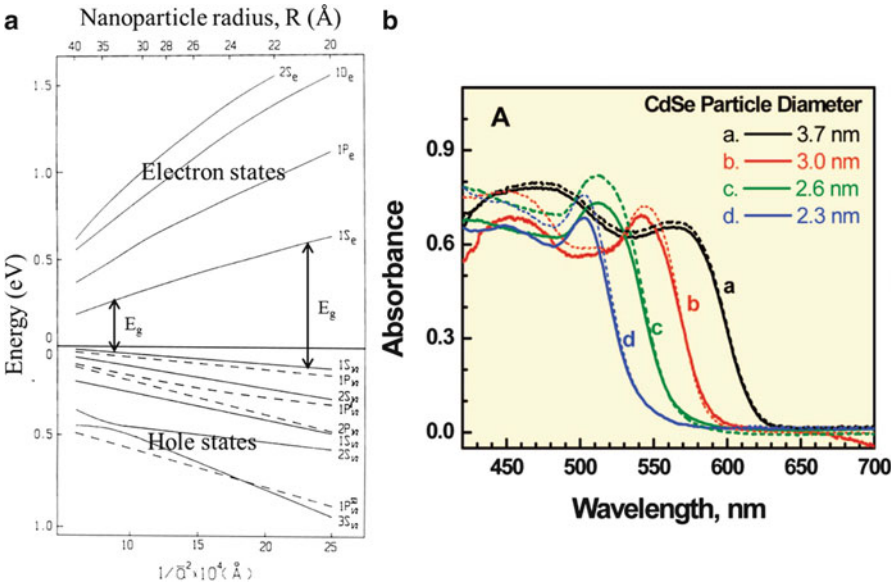

Fig. 2.1 (**a**) Theoretical size dependence of the electron and hole levels in CdSe nanocrystals. (**b**) Absorption spectra of 3.7, 3.0, 2.6, and 2.3 nm diameter CdSe quantum dots anchored on nanostructured TiO_2 films

time-independent Schrödinger equation. For a three-dimensional box, the wavefunctions and energies are given by the following equations:

$$\Psi_{n_x,n_y,n_z} = \sqrt{\frac{8}{L_x L_y L_z}} \sin\left(\frac{n_x \pi x}{L_x}\right) \sin\left(\frac{n_y \pi y}{L_y}\right) \sin\left(\frac{n_z \pi z}{L_z}\right) \tag{2.1}$$

$$E_{n_x n_y n_z} = \frac{h^2 \pi^2}{2m} \left[\left(\frac{n_x}{L_x}\right)^2 + \left(\frac{n_y}{L_y}\right)^2 + \left(\frac{n_z}{L_z}\right)^2 \right] \tag{2.2}$$

where the three-dimensional wavevector is

$$\mathbf{k}_{n_x,n_y,n_z} = k_{n_x}\mathbf{x} + k_{n_y}\mathbf{y} + k_{n_z}\mathbf{z} = \frac{n_x \pi}{L_x}\mathbf{x} + \frac{n_y \pi}{L_y}\mathbf{y} + \frac{n_z \pi}{L_z}\mathbf{z} \tag{2.3}$$

where L is the length of the box and $\mathbf{x}$, for example, denotes a unit vector along x-direction. If an exciton is a spherical particle, the relationship between energy and radius of a particle is given by

$$E^{\mathrm{e,h}} \propto \frac{1}{R^2} \tag{2.4}$$

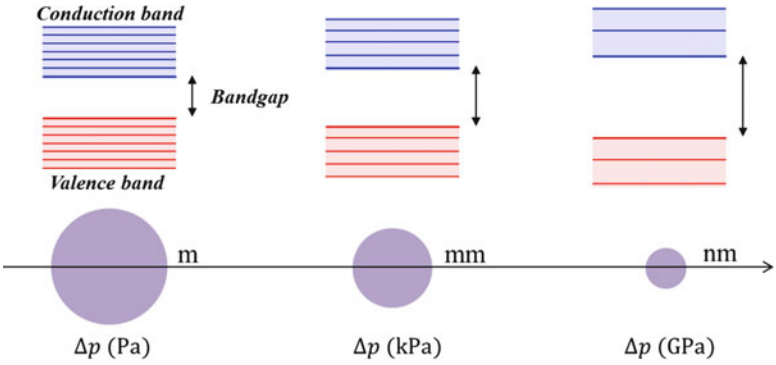

Fig. 2.2 The relationship between the band gap and the particle size explained through Young–Laplace law in the classical mechanics

On the other hand, the relation between the band gap and the particle size can also be explained by the classical Laplace–Young equation, namely,

$$\Delta p = 2\gamma H = \gamma\left(\frac{1}{R_1} + \frac{1}{R_2}\right) = \frac{2\gamma}{R} \propto \frac{1}{R} \quad \text{when } R_1 = R_2 = R \tag{2.5}$$

where Δp is the pressure difference across the fluid interface, γ is the surface tension, H is the mean curvature, and R_1 and R_2 are the two principal radii of curvature. The increase in pressure at the nanoscale results in strong forces toward the interior of the particle. This variation is responsible for the changes in inter-atomic interactions and the band gap [16, 17], as schematically represented in Fig. 2.2. Therefore, panchromatically-light-absorbing quantum-dot-sensitized solar cells can be designed by suitably exploiting the band gap engineering of the quantum-dots.

2.2.2 *Multiple Exciton Generation (=Carrier Multiplication)*

MEG involves the generation of electron–hole pairs per single photon. MEG may considerably enhance the energy conversion efficiency of QDSSCs. The energy gap between electron states is too small to be ignored because the bulk semiconductor has many atoms in total volume. Thus, excited carriers are rapidly relaxed with low phonon energy. That is, the photon energy in excess of the band gap is lost as heat through phonon emission following electron–phonon scattering when photon energy higher than band gap stimulates semiconductor materials (in Fig. 2.3a) [18–20]. The higher threshold photon energy is required for impact ionization, the process in a material by which one energetic charge carrier can lose energy by

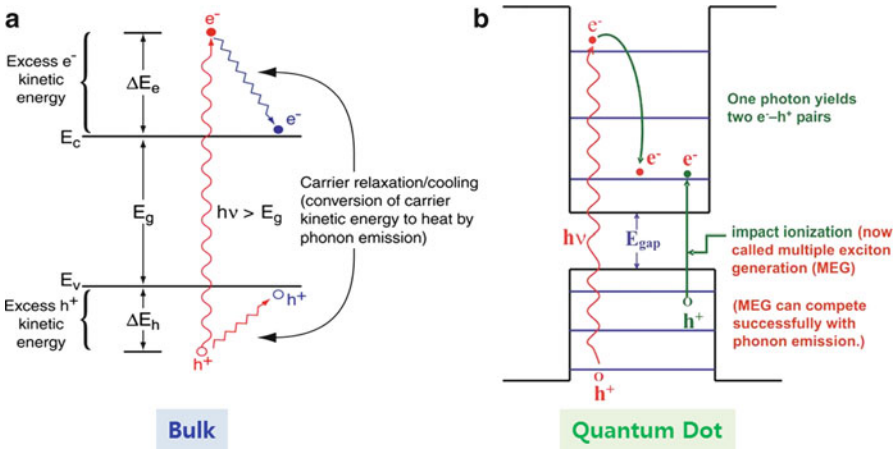

Fig. 2.3 (**a**) Hot carrier relaxation/cooling in bulk semiconductors. (**b**) Multiple electron–hole pair (exciton) generation (MEG) in quantum dots

the creation of other charge carriers, because crystal momentum (**k**) has to be conserved. This results in a low maximum quantum yield [21, 22].

On the other hand, a quantum-dot (QD) has 100–10,000 atoms in total volume. It is known that the energy separation between quantized levels in QDs can be many times higher than the phonon energy. In the relaxation process, several phonons should be emitted via electron–phonon scattering to meet the energy conservation, which accompanies multi-particle scattering events. As a result, the rate of excited electron relaxation can be retarded by the existence of discrete quantized energy levels. The slowed relaxation of hot excitons via phonon emission allows other channels for relaxation, such as MEG, to become competitive and even dominant in QDs (in Fig. 2.3b) [23]. Furthermore, the crystal momentum need not be conserved because the momentum is not a good quantum number for three-dimensionally confined carriers (from the Heisenberg Uncertainty Principle, the well-defined location of the electrons and holes in the nanocrystal makes the momentum uncertain). This results that the maximum quantum yield is very high because the lower threshold photon energy than bulk semiconductor is required for the impact ionization [24].

The difference in carrier multiplication (CM) thresholds observed in various quantum dots can be understood easily by using effective masses in simple bulk semiconductors without bringing up an exact structure of quantized states in these materials [25]. If one assumes that the energy required for an additional exciton is given by either the electron or the hole of an original exciton, then the CM threshold ($\hbar\omega_{CM}$) can be determined from the condition $\Delta E_{e(h)} = E_g$, where $\Delta E_{e(h)}$ is the energy of the electron (hole) excited by the photon in excess of the energy gap. This condition yields the following equation:

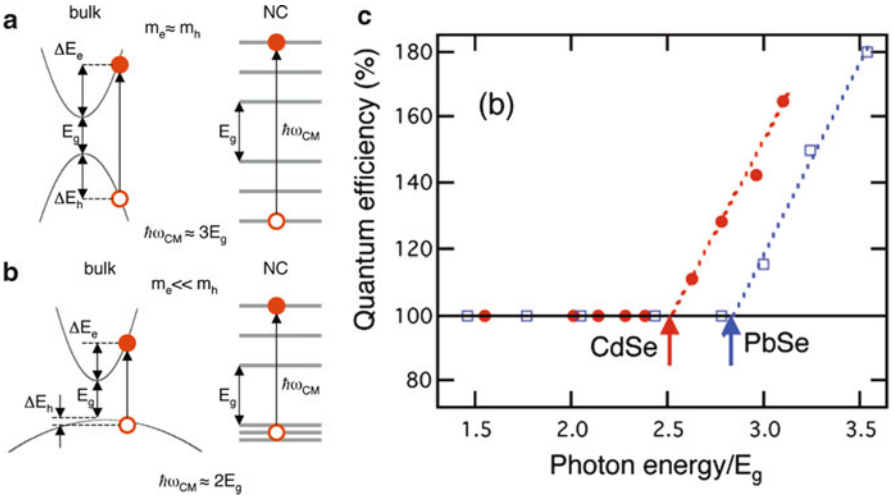

Fig. 2.4 "Bulk-like," carrier effective-mass considerations indicate that in the case of similar electron and hole masses ($m_e \approx m_h$) the onset of CM is 3.0 E_g (**a**), whereas it approaches 2.0 E_g (**b**) in the case for which the electron and hole masses are very dissimilar ($m_e \ll m_h$). (**c**) CM quantum efficiencies for CdSe (*solid circles*) and PbSe (*open squares*) nanocrystals as a function of excitation photon energy divided by E_g. The *two arrows* mark the onsets of CM

$$\hbar\omega_{CM} = \left(2 + \frac{m_e}{m_h}\right) E_g \tag{2.6}$$

In Eq. (2.6), it is assumed that $m_e \leq m_h$. In the lead salts, $m_e \approx m_h$ and hence $\hbar\omega_{CM} = 3E_g$ (Fig. 2.4a), which is consistent with the ~$3E_g$ threshold observed experimentally for PbSe nanocrystals (Fig. 2.4c). Because holes are heavier than electrons in CdSe, $\hbar\omega_{CM}$ should be smaller than $3E_g$ (Fig. 2.4b), which is again consistent with the experimental results that indicate a CM threshold of approximately $2.5E_g$ (Fig. 2.4c) [25].

2.2.3 *Molar Extinction Coefficient (=Molar Absorptivity)*

The concept of molar absorptivity is useful in analyzing optical data of sensitized solar cells. Let us first define the transmittance (T) to introduce this quantity. The ratio of radiant power transmitted (I) by a sample to the radiant power incident (I_0) on the sample is called the transmittance T:

$$T = I/I_0 \tag{2.7}$$

On the other hand, the absorbance (A) is defined by

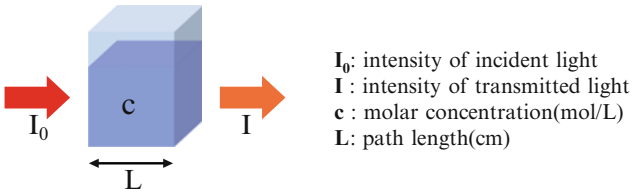

Fig. 2.5 Diagram of Beer–Lambert absorption

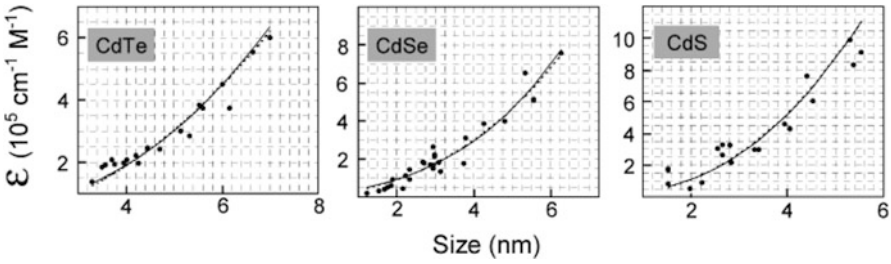

Fig. 2.6 Size-dependent extinction coefficient per mole of nanocrystals at the first excitonic absorption, ε, of CdTe, CdSe, and CdS nanocrystals

$$A = -\log T = \log(1/T) \tag{2.8}$$

The transmittance and absorbance depend on the molar concentration (c), light path length in centimeters (L), and molar absorptivity ($\boldsymbol{\varepsilon}$) for the dissolved substance [26].

$$T = 10^{-\varepsilon cL} \quad \text{or} \quad A_\lambda = \varepsilon cL \tag{2.9}$$

Beer's Law states that the molar absorptivity is constant and the absorbance is proportional to the concentration for a given substance dissolved in a given solute and measured at a given wavelength [27]. Since transmittance and absorbance are unitless, the units for molar absorptivity must cancel with units of measure in concentration and light path. Accordingly, the unit for molar absorptivity has M^{-1} cm^{-1} or L mol^{-1} cm^{-1}. Most of laboratory spectrophotometers are fitted for use with 1 cm width cuvettes. Thus, molar absorptivity is expressed as

$$A_\lambda = \varepsilon cL = \varepsilon c \quad \text{when } L = 1 \text{ cm} \tag{2.10}$$

The molar extinction coefficient values of quantum dots (such as CdS, CdSe, and CdTe) are ~10^5 cm^{-1} M^{-1} (Fig. 2.6) [2], an order of magnitude higher than ~10^4 cm^{-1} M^{-1} (Table 2.1) of ruthenium(II) complexes (such as N3 and N719) [4]. This implies that QDSSCs can absorb more light than DSSCs do at similar film thickness.

Table 2.1 Electronic spectral data of ruthenium(II) complexes

Complex	Adsorption λ(max) (nm) ($\epsilon/10^4$ M^{-1} cm^{-1})		
$[Ru(dcbpyH_2)_2(cl)_2]$	565 (1.1)	414 (1.0)	316 (3.45)
$[Ru(dcbpyH_2)_2(NCS)_2]$	538(1.42)	398 (1.40)	314 (4.82)
$(Bu_4N)_4[Ru(dcbpyH_2)_2(NCS)_2]$	518 (1.3)	380 (1.33)	308 (4.59)
$(Bu_4N)_2[Ru(dcbpyH_2)_2(NCS)_2]$	535 (1.47)	395 (1.43)	312 (4.91)

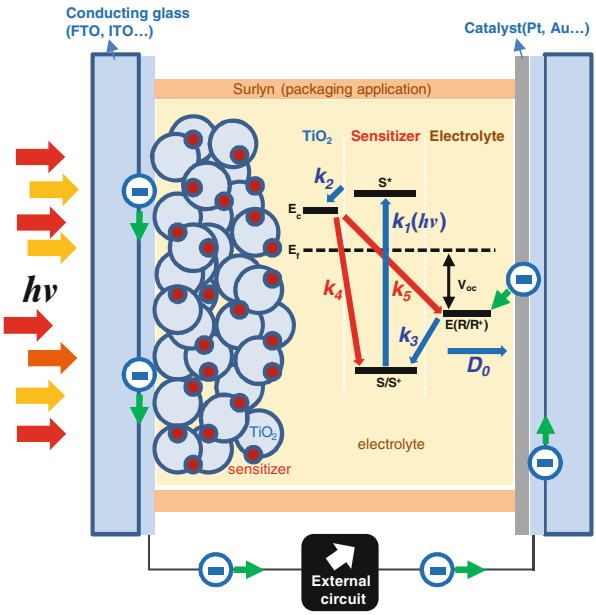

Fig. 2.7 The major kinetic processes in the operation of a QDSSC device

2.2.4 Kinetic Processes Occurring in a QDSSC

The energetics and key kinetic processes occurring in a QDSSC are illustrated in Fig. 2.7. Light is absorbed by quantum dots attached to the surface of a TiO_2 nanoparticle (k_1). The excited dye injects fast an electron into the TiO_2 conduction band (k_2) which is the source of the photocurrent. A redox shuttle in solution is required for the regeneration of the dye (k_3); diffusion of the oxidized form of the redox shuttle (D_o) to be reduced at the counter electrode completes the circuit. These processes compete with several reactions that inhibit the efficient operation of a QDSSC including decay (either radiative or nonradiative) of the chromophore's excited state as well as back-electron transfer from the TiO_2 nanoparticle to the oxidized dye (k_4) or the oxidized form of the redox shuttle (k_5). For a QD-sensitized DSSC, the decay of the QDs in an I^-/I_3^- redox system causes a rapid decrease of the photocurrent. For the QDSSCs using cadmium chalcogenides

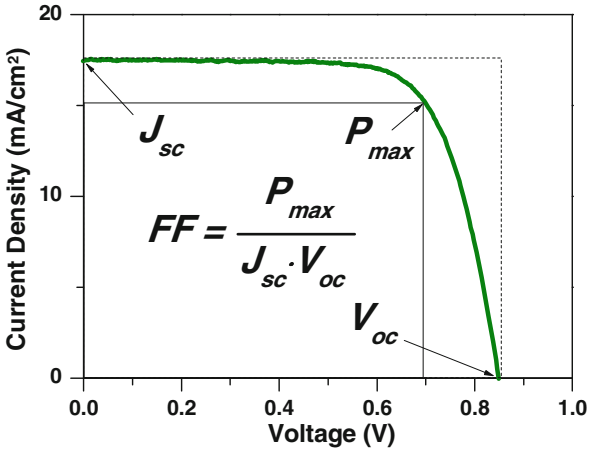

Fig. 2.8 Photocurrent density vs. voltage curve and the equation for fill factor

(S, Se or Te) as sensitizers, redox couple of polysulfide (S_2^{-}/S_x^{2-}) is a suitable system for stabilizing the QDs [28].

The power conversion efficiency of a solar cell, η, is usually expressed as

$$\eta = \frac{P_{\max}}{P_{\text{in}}} = \frac{J_{\text{sc}} \cdot V_{\text{oc}} \cdot \text{FF}}{P_{\text{in}}} \tag{2.11}$$

where $P_{\max}$ and P_{in} are the maximum electrical power output and the incident solar power, respectively. The short circuit photocurrent density (J_{sc}) is the cell current measured at an applied potential of 0 V. J_{sc} is a function of the illumination intensity. The open-circuit photovoltage (V_{oc}) is the difference between the Nernstian potential of the solution, $E(\text{R}/\text{R}^{+})$, and the quasi-Fermi level, E_{f} (i.e., potential of the semiconductor), and the fill factor (FF) is a term introduced to relate $P_{\max}$ to the parameters J_{sc} and V_{oc}, corresponding to the ratio of the area under a J–V curve defined by $P_{\max}$ to the area defined by J_{sc} and V_{oc} (Fig. 2.8).

2.3 Experimental Backgrounds

2.3.1 Electrochemical Impedance Spectroscopy (EIS)

EIS is used to analyze internal resistance in QDSSCs. Resulting impedance spectra can be fitted to an appropriate equivalent circuit, as shown in Fig. 2.9a [29–31]. In general, at least three internal resistances are found. Figure 2.9b shows a Nyquist plot. The three semicircular shapes are assigned to impedances related to charge transport at the Pt counter electrode (Z_{Pt}) in the high-frequency region (10^3–10^5 Hz), at the TiO_2/QD/electrolyte interface (Z_{ct}) in the middle-frequency region (10^0–10^3 Hz), and in the Warburg diffusion within the electrolyte (Z_{d}) in the

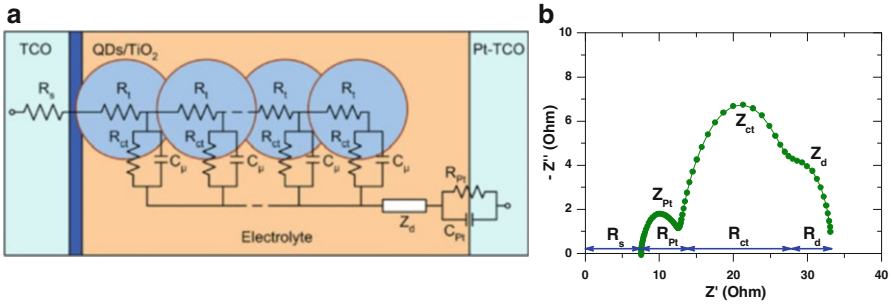

Fig. 2.9 (**a**) Equivalent circuit used to fit the EIS spectra. (**b**) A Nyquist plot taken showing each resistive element

low-frequency region (10^{-2}–10^{0} Hz), respectively. The resistance elements R_{Pt}, R_{ct}, and R_d are described as the real parts of Z_{Pt}, Z_{ct}, and Z_d, respectively [32]. R_s is the series resistance of the cell including the TCO sheet resistance and R_T is the electron transport resistance through the nanoparticle TiO_2 film.

The frequency (f) at maximum imaginary components of each semicircle in a Z''–Z' plot is the reciprocal of time constant (τ) for an equivalent circuit. Thus, the recombination lifetime (τ_r) between the electrons in the TiO_2 and the oxidized form of the redox couples in the solution can be calculated by adopting the following equation [33].

$$\tau_r = \frac{1}{\omega_{max}} = \frac{1}{2\pi f} \tag{2.12}$$

where ω_{max} refers to the peak frequency of the second semi-arc related to R_{ct}.

2.3.2 *Intensity-Modulated Photocurrent/Photovoltage Spectroscopy (IMPS/IMVS)*

One of the parameters that determine the photocurrent density is the charge-collection efficiency (η_{cc}). η_{cc} can be determined by the IMPS/IMVS. In brief, the IMPS measures the periodic current response to the intensity-modulated light, providing kinetic information on the charge transport under short-circuit conditions. The IMVS experiment is conducted with the same perturbed light but under open-circuit conditions, which offers the recombination lifetime. The electron transport time (τ_t) can be estimated using the equation $\tau_t = 1/(2\pi f_t)$, where f_t is the characteristic frequency minimum of the IMPS imaginary component. Similarly, the recombination lifetime (τ_r) can be determined using the relation of $\tau_r = 1/(2\pi f_r)$, where f_r is the characteristic frequency minimum of the IMVS imaginary component.

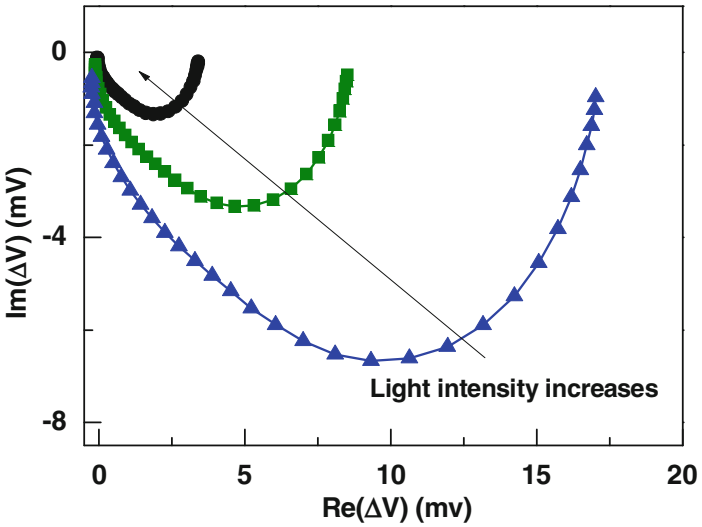

Fig. 2.10 IMVS measurements performed at different DC light intensities

As shown in Fig. 2.10, the semi-circle radius decreases with increasing light intensity. The frequency corresponding to the minimum in the complex plane increases as the light intensity increases, which indicates that the electron lifetime decreases. Therefore, the electron recombination is more pronounced at high illumination intensities. The IMPS data are similar to the data obtained in the IMVS measurements. At high frequencies the modulated photocurrent approaches zero, indicating that the modulation frequency is faster than the relaxation of the charge carrier density by transport to the contacts and back reaction.

The charge-collection efficiency (η_{cc}), electron diffusion coefficient (D_n), and effective electron diffusion length (L_n) can be calculated by the two values obtained from the above IMPS and IMVS analysis via the following equations [34, 35]:

$$\eta_{cc} = 1 - \frac{\tau_t}{\tau_r} \tag{2.13}$$

$$D_n = \frac{L^2}{(2.35\tau_t)} \tag{2.14}$$

where L is film thickness.

$$L_n = (D_n \times \tau_r)^{1/2} \tag{2.15}$$

2.4 Novel Nanostructured Photoelectrodes for Efficient QDSSCs

2.4.1 Tertiary Hierarchically Structured TiO_2 for CdS QDSSCs

Recently, tertiary-hierarchically-structured mesoporous spherical TiO_2 (MS TiO_2) was proposed as an alternative to the traditional nanoparticle photoelectrode in the QDSSCs [12]. MS TiO_2 particles have a mean diameter of 1,190 ± 60-nm, which consists of ~100-nm-sized secondary particles formed by clustering of 15-nm-sized primary nanocrystallites. In addition to the dual function of high loading capacity and scattering effect, accessible pores of the MS TiO_2 were successfully utilized for efficient CdS QDSSCs. The large external pores formed by the stacking of micrometer particles can offer direct paths for the diffusion of metal and chalcogen ions in a SILAR (successive ionic layer adsorption and reaction) process [36]. A conversion efficiency of 1.9 % was achieved by CdS QDSSCs composed of MS TiO_2 photoanode, noticeably higher than 1.2 % for conventional QDSSCs made of 20-nm-sized nanocrystalline TiO_2 (Solaronix, T20) and those of other reported CdS QDSSCs: 1.15 % with nanocrystalline TiO_2 film [28], 1.2 % with TiO_2 nanospheroidal electrodes [37], 1.46 % with ZnO nanotubes [38].

Figure 2.11a shows a morphological feature of the calcined MS TiO_2 particles. The high-magnification FE-SEM image indicates that the MS TiO_2 particles possess a tertiary hierarchical structure: the particles are composed of ~100-nm-sized secondary particles which, in turn, are made up of ~15 nm-sized primary nanocrystallites. It is observed that the CdS QDs are more thickly deposited with better surface coverage, forming agglomerates on the MS TiO_2 (Fig. 2.11b). In comparison, SEM images of the commercial nanocrystalline T20 film before and after the deposition of the CdS QDs are shown in Fig. 2.11c, d. As shown in the insets of Fig. 2.11, the MS TiO_2 has large external pores due to the stacking of micrometer-sized spherical colloids. On the other hand, T20 particles seem to be densely packed, thereby leaving only tiny mesopores. The following STEM analysis reveals more detailed information on the deposited CdS QDs grown after 12 SILAR cycles, where the SILAR (successive ionic layer adsorption and reaction) technique [36] is known as a modified version of chemical bath deposition.

Figure 2.12 shows the STEM images of the CdS QD-sensitized T20 (a, b) and MS TiO_2 (c, d) particles. The crystal size of the QDs is about 3–5 nm for both MS TiO_2 and T2 samples. However, the MS TiO_2 sample seemingly forms larger CdS agglomerates with better coverage on the TiO_2 surface. In contrast, most of the QDs seem to be individual on the T20 surface with less agglomeration of QDs, and partially uncovered surface is also found. This implies that the surface coverage of the QDs is relatively superior at the MS TiO_2 surface. As a result, the thickness of the CdS layer is estimated to be about 6.5–9.5 nm for the MS TiO_2 sample, whereas the thickness is nearly a half for the T20 (~3–6 nm). Electron energy loss

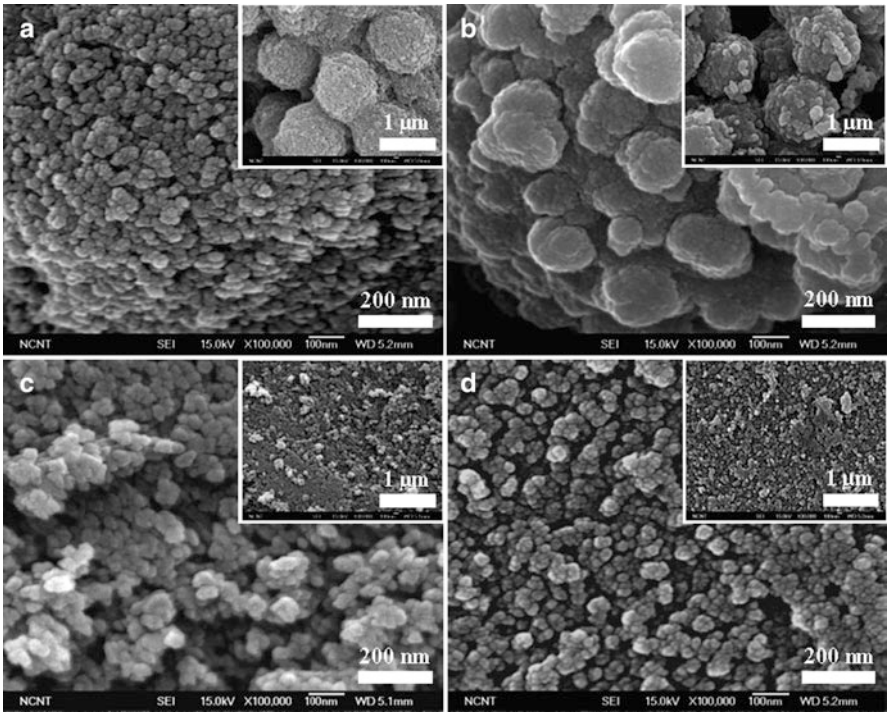

Fig. 2.11 *Top-view* images of the calcined MS TiO_2 film (**a**) before and (**b**) after CdS QD deposition, in comparison with those of the T20 film (**c**) before and (**d**) after CdS QD deposition

spectroscopy (EELS) was conducted to analyze the spatially resolved composition of the sensitized MS TiO_2 sample at a high resolution. A magnified TEM image of a single MS TiO_2 particle and corresponding EELS data are shown in Fig. 2.12e, f. It is clear that the CdS QDs are evenly distributed within an MS TiO_2 particle [12].

The X-ray diffraction patterns of the calcined TiO_2 films without and with SILAR process are presented in Fig. 2.13. After solvothermal treatment and subsequent calcination, well-resolved diffraction peaks appear as shown in Fig. 2.13a, which indicates the crystallization to anatase TiO_2 (JCPDS card No. 21-1272). From the XRD pattern presented in Fig. 2.13c, it can be concluded that the sintered T20 particles also exist in the anatase form. The average crystallite sizes of the calcined MS TiO_2 and T20 were 14.71 and 19.99 nm, respectively, as estimated from the full-width at half-maximum (FWHM) of the anatase (1 0 1) peak using the Scherrer equation. Figure 2.13b, d presents the XRD patterns taken after the CdS QD deposition with 12 SILAR cycles on the MS TiO_2 and the T20 films, respectively. It is confirmed that the CdS QDs are formed with a cubic structure according to the JCPDS card no. 80-0019. The crystal size was calculated from the FWHM of the CdS (1 1 1) peak. The diameter of the CdS QDs is estimated to be ~2.6 nm for both MS TiO_2 and T20.

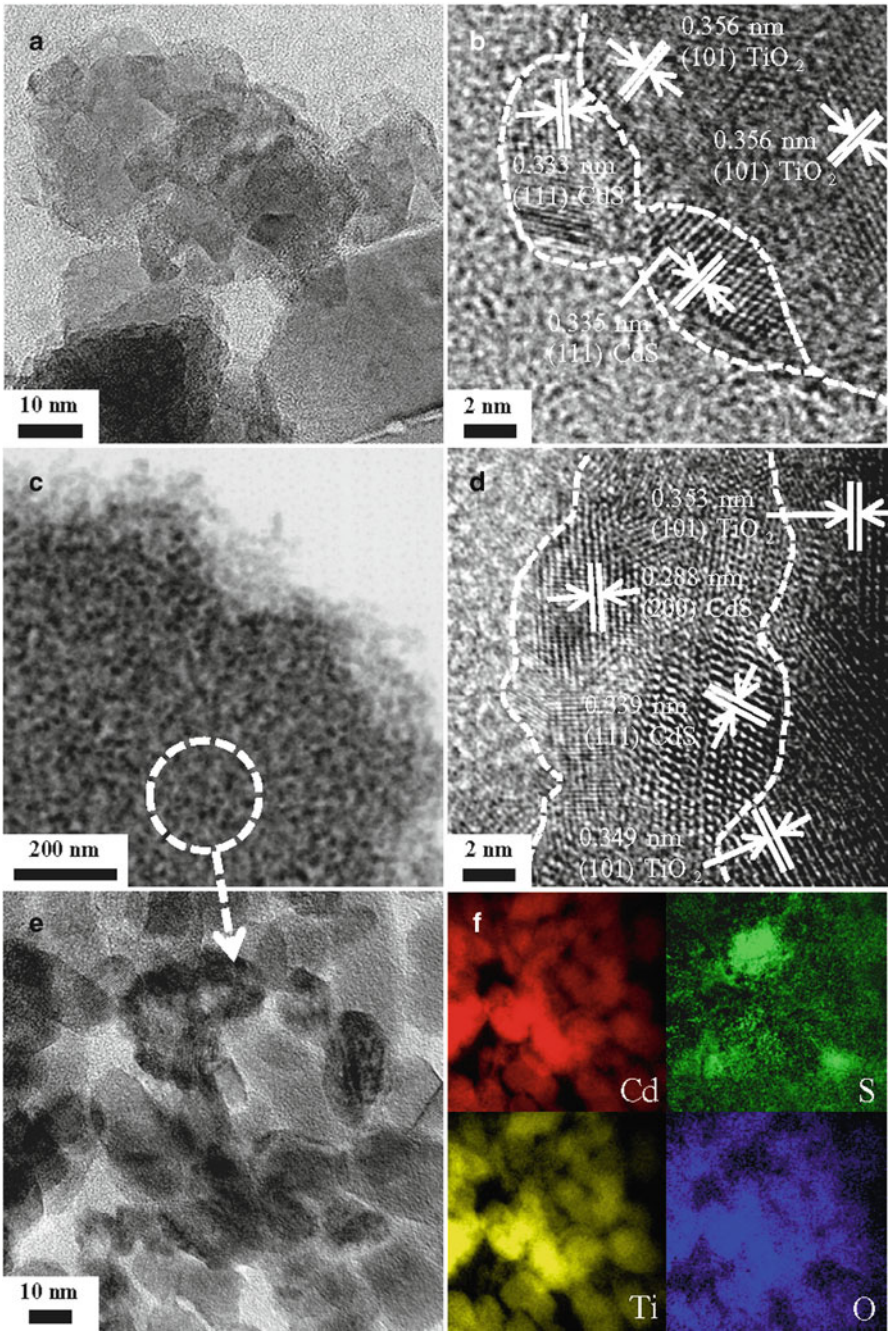

Fig. 2.12 STEM images of the CdS QD-sensitized TiO_2 particles. (**a**, **b**) T20 particles after SILAR process (**c**, **d**) A sliced MS TiO_2 particle after SILAR process (**e**, **f**) A high resolution TEM image of the sensitized MS TiO_2 particle, and corresponding EELS data

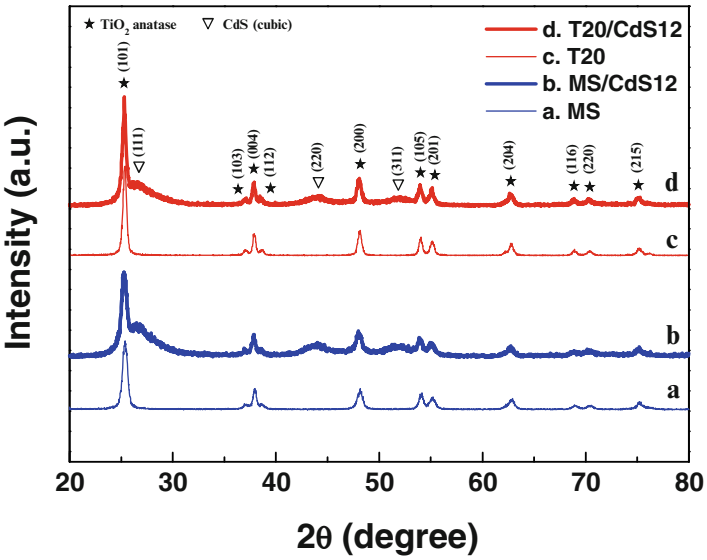

Fig. 2.13 XRD patterns of the calcined MS TiO_2 without (**a**) and with (**b**) SILAR process, and the calcined T20 without (**c**) and with (**d**) SILAR process

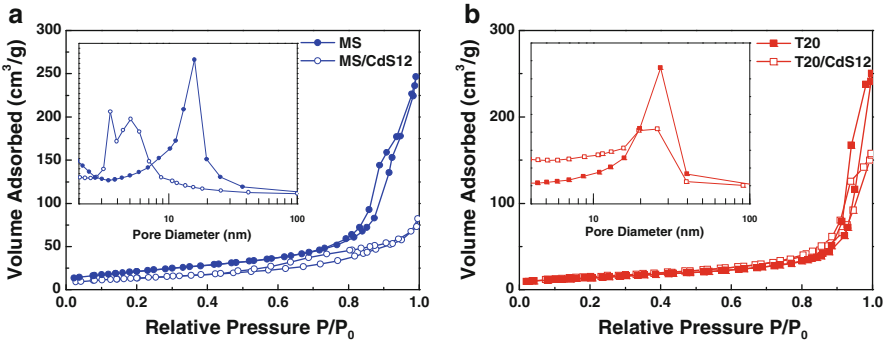

Fig. 2.14 Nitrogen sorption isotherms of the calcined MS TiO_2 (**a**) and the T20 (**b**) without and with SILAR process. The *inset* shows the corresponding pore-size distribution for both samples, as estimated by BJH analysis

The specific surface area and the pore-size distribution were characterized by measuring nitrogen-gas-sorption isotherms (Fig. 2.14a, b). For both MS TiO_2 and T20, H1-type hysteresis loops [39] and type IV isotherms with sharp capillary-condensation steps at a high relative pressure were observed. However, the estimated average pore size of each particle is markedly different: 15.9 nm for the MS TiO_2 and 26.9 nm for the T20. The specific surface area of the MS TiO_2 is estimated to be 76.02 $m^2\ g^{-1}$ which is about 1.5 times higher than that of the T20 (49.05 $m^2\ g^{-1}$). After the CdS QD deposition, the surface area of the MS TiO_2 is

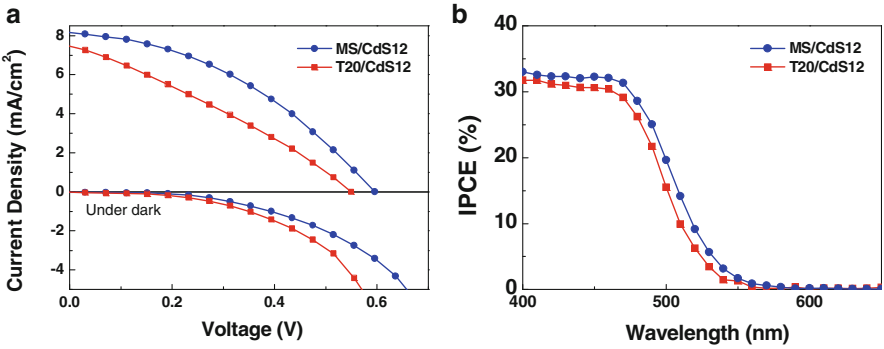

Fig. 2.15 (**a**) *I–V* and (**b**) IPCE (chopping frequency = 10 Hz) curves of CdS QDSSCs with the MS TiO_2 and the T20

greatly reduced to 48.52 $m^2\ g^{-1}$, whereas that of the T20 does not change much. Therefore, it can be inferred that the CdS QDs are deposited on the primary pores of the MS TiO_2 particles with good surface coverage, leading to a significant decrease in the surface area and the pore size. It is also confirmed that the primary pores still have a finite size, which can provide available sites for the interfacial reaction with the electrolyte. This assumption is in good agreement with the previous analysis obtained from the SEM and TEM images.

The current–voltage characteristics of the QDSSCs were studied under one sun illumination and dark condition (Fig. 2.15a). With the CdS QDs grown after 12 SILAR cycles, the MS TiO_2 cell performed the maximum efficiency of 1.9 %, which corresponds to ~58 % enhancement, as compared with the value obtained from the T20 cell (1.2 %). The increased efficiency of the MS TiO_2 cell is mainly attributed to the higher fill factor (FF) and the short-circuit photocurrent (J_{sc}). FF of each cell is reflected on the dark current–voltage curve. Since the dark current measured for the MS TiO_2 cell is relatively less, it can be concluded that the charge recombination is somewhat reduced in the MS TiO_2 cell.

As shown in Fig. 2.15b, the quantum efficiency (IPCE; incident-photon-to-current conversion efficiency) is also higher in the MS TiO_2 cell over the whole spectral range, as compared with that of the T20 cell. The improved photocurrent observed in QDSSCs with the tertiary-hierarchically-structured MS TiO_2 photoanode can be attributed to (a) the high surface area for QD loading and (b) the light scattering effect confirmed by the diffuse reflectance spectra presented in Fig. 2.16a. Owing to the presence of micrometer-sized tertiary colloidal particles, the MS TiO_2 is revealed to effectively scatter visible light (400–800 nm), which results in improved photovoltaic performances. The inset of Fig. 2.16a shows the difference in the transparency between the MS TiO_2 and T20. After the sensitization with the CdS QDs grown after 12 SILAR cycles, the reflectance spectra take on a new aspect (Fig. 2.16b): the reflectance of each sample is greatly reduced at the short wavelength range (<550 nm) due to the absorption of the incident light by the

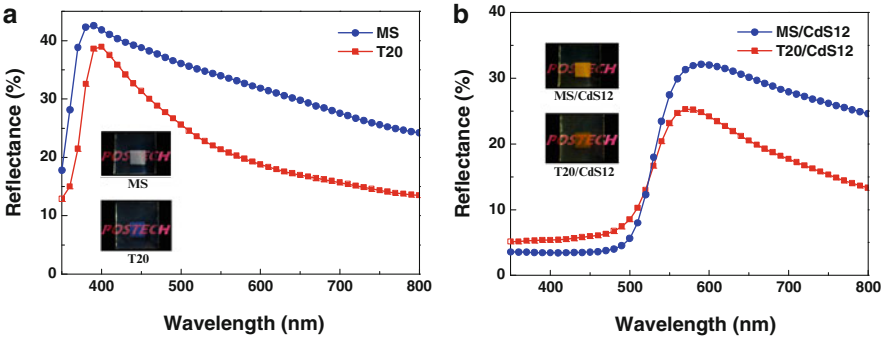

Fig. 2.16 Diffuse reflectance spectra of the CdS QD-sensitized MS TiO_2 and the T20 films (**a**) without and (**b**) with the SILAR process. The each *inset* compares *top-view* images of these two photoanodes

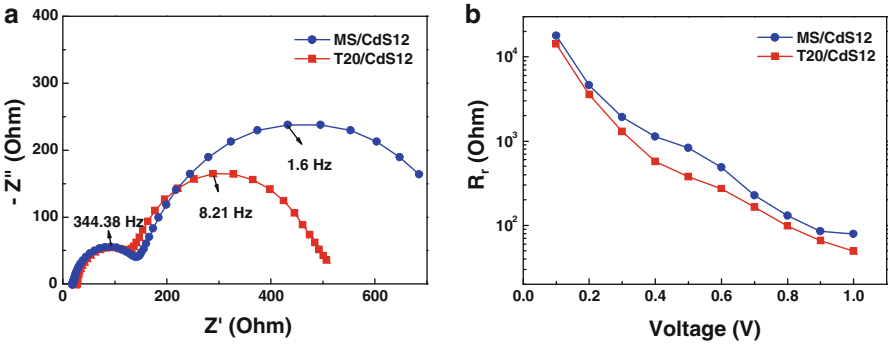

Fig. 2.17 (**a**) Nyquist plots of the EIS spectra and (**b**) R_{ct} for CdS QDSSCs with the MS TiO_2 and the T20 under dark

CdS QDs. As shown in the inset of Fig. 2.16b, the CdS QD-sensitized MS TiO_2 film is opaque with a tint of orange color while the sensitized T20 film is transparent [12].

The EIS was employed to examine the interfacial reactions in QDSSCs (Fig. 2.17). Typical Nyquist plots of both cells were obtained at the V_{oc} condition under dark using the equivalent circuit shown in the inset of Fig. 2.17a. τ_r is estimated to be 625 and 122 ms for the MS TiO_2 and the T20 cells, respectively. Figure 2.17b shows R_{ct} (charge recombination resistance) for both cells which decreases with increasing applied voltage [40]. It is shown that the MS TiO_2 cell has higher R_r than the T20 cell at various applied voltages. This result implies that the dark current arising from the recombination is greatly suppressed at the MS TiO_2/polysulphide electrolyte interface, which offers a higher V_{oc}, FF, and improved conversion efficiency. We attribute the reduced interfacial recombination

reaction to the better coverage of CdS QDs [41]. Since the large external pores observed in the MS TiO_2 particles promote a fast diffusion of precursor ions in a SILAR process, CdS QDs are expected to be deposited well on the MS TiO_2 film.

2.4.2 *Sea Urchin TiO_2–Nanoparticle Hybrid Composite Photoelectrodes for CdS/CdSe/ZnS QDSSCs*

Hierarchically-structured materials are composed of nanocrystallites that are aggregated to form large secondary spheres, thereby can provide efficient light scattering with maintaining a large surface area for sufficient sensitizer-uptake. Although these 0–3 hierarchical materials can be a good alternative to the traditional nanocrystalline TiO_2, slow trap-limited charge transport remains a fundamental problem. To overcome this limit, a different type of hierarchical nanostructures was developed: sea urchin TiO_2 (SU TiO_2) formed by clustering nanowires that has a mean diameter of about 50 nm and a length of a few micrometers to construct a radially aligned particle that is 4–7 μm in diameter (1–3 hierarchy). It has been widely reported that nanowire-based structures have superior electron lifetime and recombination time than traditional nanoparticle films. In addition to the advantage of charge collection efficiency, nanowires can effectively scatter visible light, thereby enhancing the overall light harvesting.

A new approach implemented the benefits of one-dimensional nanostructures by suitably combining the SU TiO_2 and traditional TiO_2 nanoparticles (NP) to construct a hybrid composite photoelectrode (SU–NP) for the QDSSCs. In particular, the nanoparticles offer a high surface area (~75 $m^2\ g^{-1}$) for sufficient QD loading, whereas SU TiO_2 particles provide a highway for fast charge collection and multiple scattering centers within the photoelectrode (Fig. 2.18). CdS/CdSe/ZnS QDSSCs made of the SU–NP composite film exhibited remarkable improvement in power conversion efficiency: 4.2 versus 3.5 % for the reference cell made with the NP film [42].

Figure 2.19a–c shows morphological features of the calcined SU TiO_2 particles. The high-magnification FE-SEM image indicates that the SU TiO_2 particles are composed of nanowires that have a mean diameter of about 50 nm and a length of a few micrometers to construct a radially aligned particle that is 4–7 μm in diameter. In the inset of Fig. 2.19b, broken particles reveal the internal nanostructure of the SU TiO_2. It seems that many nanowires are densely packed within the spherical particle. The high-resolution image of a single nanowire constituting the SU TiO_2 (Fig. 2.19d) shows that the material is fully crystalline with the lattice spacing of 0.324 nm, which corresponds to the rutile (1 1 0) plane.

Time-dependent analysis provides more detailed information on the formation process of the SU TiO_2. Figure 2.20a shows that nanoparticles were initially created after 30 min solvothermal reaction. With the prolongation of reaction time (Fig. 2.20b, c: 1 and 1.5 h), the aggregates were formed which finally led to the

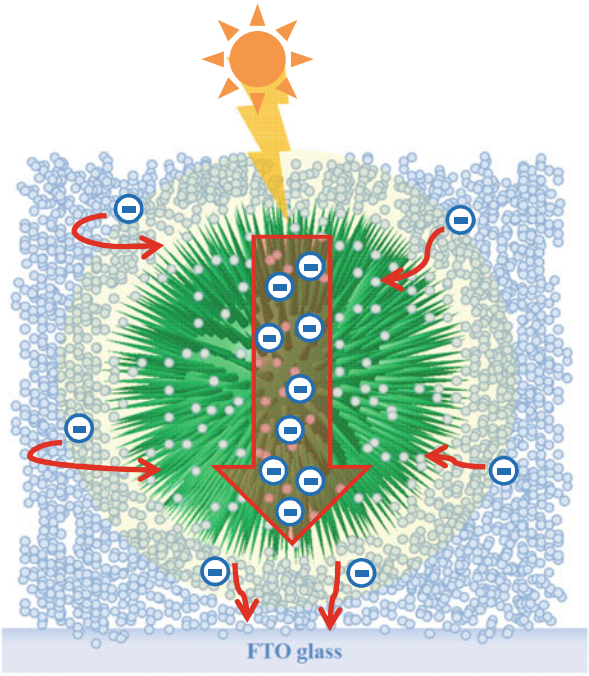

Fig. 2.18 A schematic diagram of a sea urchin TiO_2–nanoparticle composite (SU–NP) film that has fast charge collection and a light scattering effect

1–3 hierarchically-structured SU TiO_2 (Fig. 2.20d, 4 h). The anisotropic growth of nanowires on the spherical particle surface can be understood in terms of shape-controlled chemistry [43–45]. It is thought that Cl^- ions adsorb selectively onto the (1 1 0) crystal plane [46], which limit further growth of this plane, resulting in anisotropic growth and hence radially aligned TiO_2 nanowire formation.

The XRD patterns indicate that two distinct samples are in different crystalline phases (Fig. 2.21): SU TiO_2 in rutile and NP in anatase, respectively (JCPDS card Nos. 21-1276 and 21-1272).

Figure 2.22 shows the STEM images of the CdS/CdSe/ZnS QD-sensitized NP (a) and SU films (c). Most of the QDs seem to be individual on the NP film with less agglomeration of the QDs, and partially uncovered surface is also found. In contrast, the SU TiO_2 seemingly forms larger QDs agglomerates with better coverage on the surface of TiO_2 nanowires. This implies that the surface coverage of the QDs is superior at the SU TiO_2. EELS measurement was conducted to analyze the spatially resolved composition of the sensitized NP and SU TiO_2 samples at a high resolution. Magnified TEM images of NP and SU TiO_2 and the corresponding EELS data are shown in Fig. 2.22b, d.

The current–voltage characteristics of the QDSSCs were studied under one sun illumination (Fig. 2.23). The SU–NP cell shows V_{oc}, J_{sc}, fill factor (FF), and power conversion efficiency (η) of 531 mV, 18.2 mA cm^{-2}, 0.43, and 4.2 %, respectively; the reference NP cell performs 510 mV, 15.2 mA cm^{-2}, 0.45, and 3.5 %. Both J_{sc} and η of the SU–NP device are improved by around 20 %, compared to those of the

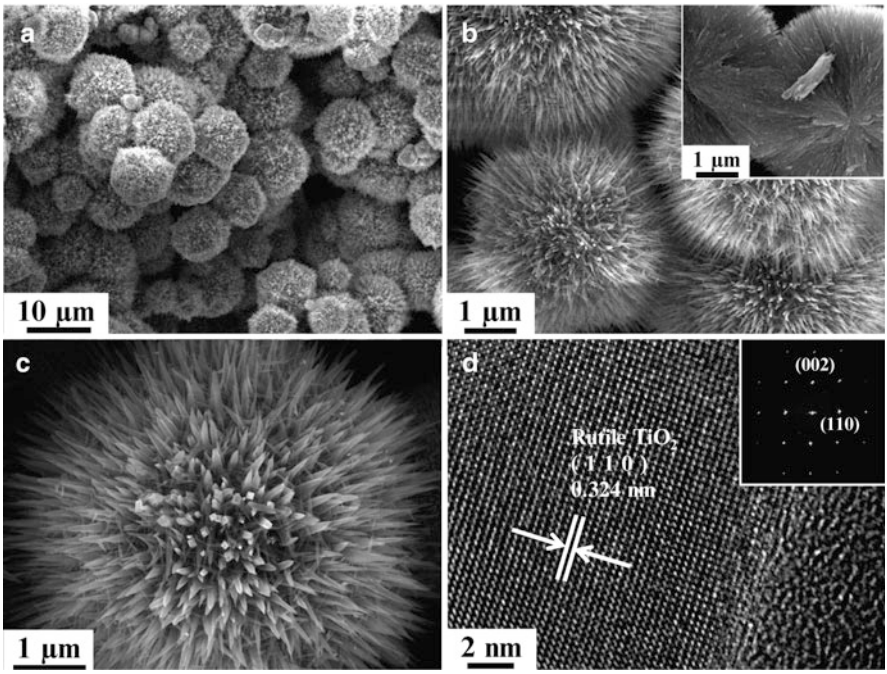

Fig. 2.19 SEM images of the SU TiO_2 particles at different magnifications (**a**, **b**, **c**). The *inset* of (**b**) shows a cross-sectional view of broken particles. A TEM image of a 1D nanocrystal in the SU TiO_2 particle (**d**). The *inset* of (**d**) shows a selected-area electron diffraction pattern

NP cell. The quantum efficiency (IPCE) provides detailed information on the light harvesting mechanism (inset of Fig. 2.23). It is observed that the overall IPCE values of the SU–NP cell are higher than the NP cell over the whole spectral range. This implies that efficiency improvement in the SU–NP composite QDSSC is mainly due to the enhanced current density.

It is well known that the photocurrent density (J_{sc}) can be calculated by the following expression [47]:

$$J_{sc} = q\eta_{lh}\eta_{inj}\eta_{cc}I_0 \tag{2.16}$$

where q is the elementary charge, η_{lh} is the light harvesting efficiency of a cell, η_{inj} is the charge-injection efficiency, η_{cc} is the charge-collection efficiency, and I_0 is the light flux. Here, η_{lh} is commonly determined by the amount of adsorbed QDs and light scattering of the films; η_{cc} is largely determined by the competition between the charge collection and recombination [34]. Since identical QDs (CdS/CdSe/ZnS) are applied to both the SU–NP and NP films, η_{inj} values of two QDSSCs are assumed to be same. Accordingly, it can be concluded that the photocurrent density in our experimental condition is determined by two parameters: the light harvesting efficiency (η_{lh}) and the charge-collection efficiency (η_{cc}).

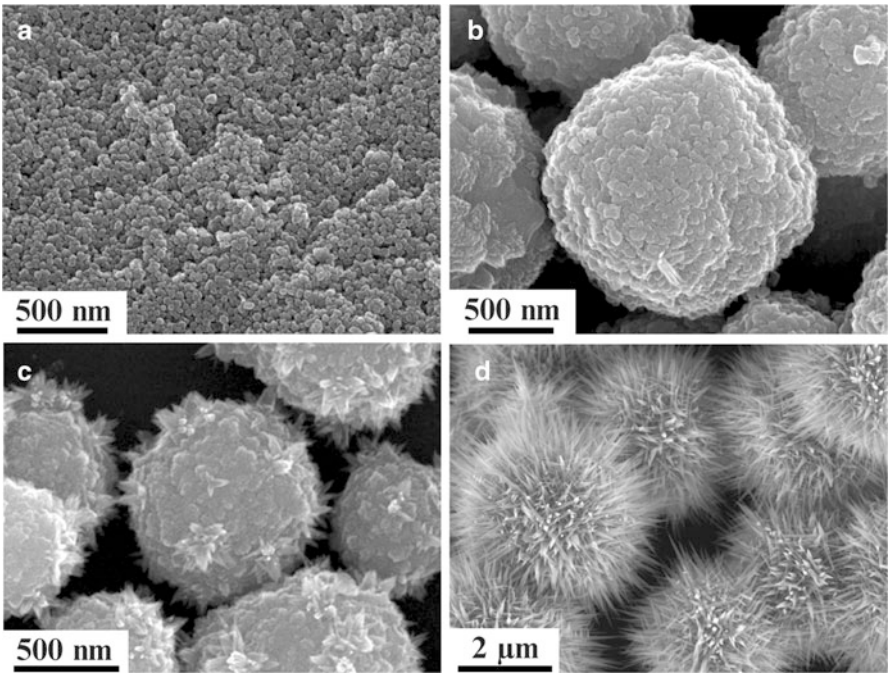

Fig. 2.20 SEM images of as-prepared SU TiO_2 at different reaction time: 30 min (**a**), 1 h (**b**), 1.5 h (**c**), and 4 h (**d**)

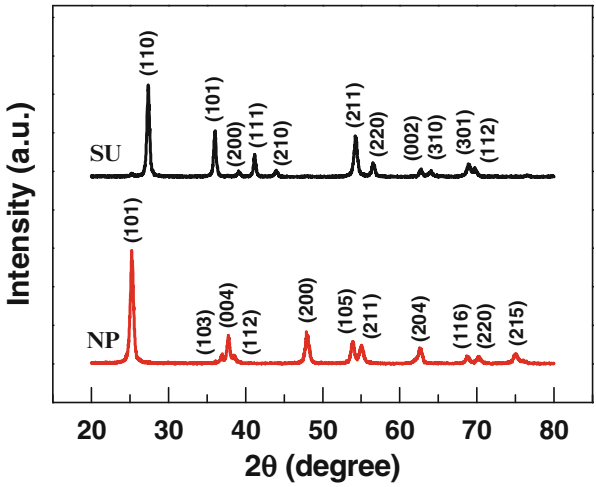

Fig. 2.21 XRD patterns of the SU TiO_2 particles and the TiO_2

The η_{lh} value is explained by the reflectance spectra. Since the micrometer-sized SU TiO_2 particles can function as scattering centers (Fig. 2.24), the SU–NP composite film can effectively confine visible light (450–750 nm). The inset of Fig. 2.25a shows the difference in the transparency of the SU–NP and NP films.

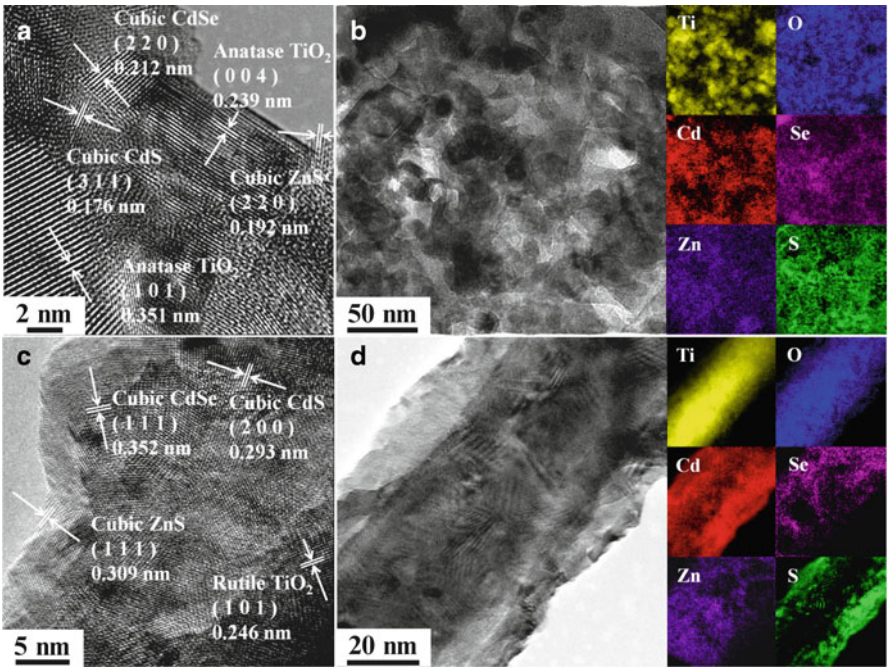

Fig. 2.22 STEM images of the CdS/CdSe/ZnS QD-sensitized TiO_2 nanocrystals. (**a**, **b**) The sensitized NP film and (**c**, **d**) SU film. Each *inset* compares EELS data of these two sensitized films

We concluded that improved red response of the NP–SU film contributes to the enhancement in the η_{lh}, which is reflected to the increased IPCE values at the long wavelength region. After the sensitization with the CdS/CdSe/ZnS QDs, the reflectance spectra take on a new aspect (Fig. 2.25b). The reflectance of each sample is reduced at the short wavelength range (under 650 nm) due to the absorption of the incident light by the QDs. As shown in the inset of Fig. 2.25b, the sensitized SU–NP film and NP film are dark red.

Even though the SU TiO_2 particles possess an inferior QD loading capacity owing to a lower surface area of 10.16 $m^2\ g^{-1}$ (NP: 73.29 $m^2\ g^{-1}$), the SU–NP device yielded remarkably larger IPCE values at the short wavelength region. This contradictory IMPS/IMVS result comes from the difference between η_{cc} in two distinct QDSSCs (SU–NP and NP cells).

Figure 2.26a presents the plot of the electron transport time (τ_t). It is noticeable that τ_t of the SU–NP hybrid composite-based QDSSC is larger than that of the reference NP cell. The relatively faster electron transport seems to be due to fewer interparticle junction within the SU–NP photoelectrode. The effective electron diffusion coefficient (D_n) of the SU–NP cell was 2.3 times larger than that of the NP cell under 100 W m^{-2} illumination (Fig. 2.26c).

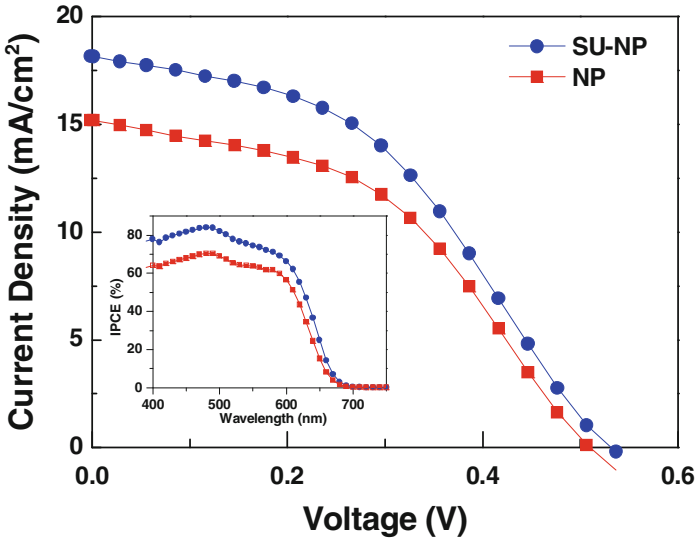

Fig. 2.23 *I–V* characteristics of the CdS/CdSe/ZnS QDSSCs with the SU–NP composite film and the reference NP film under illumination (AM 1.5, 100 mW cm^{-2}). The *inset* shows the corresponding IPCE spectra measured at chopping frequency of 3 Hz

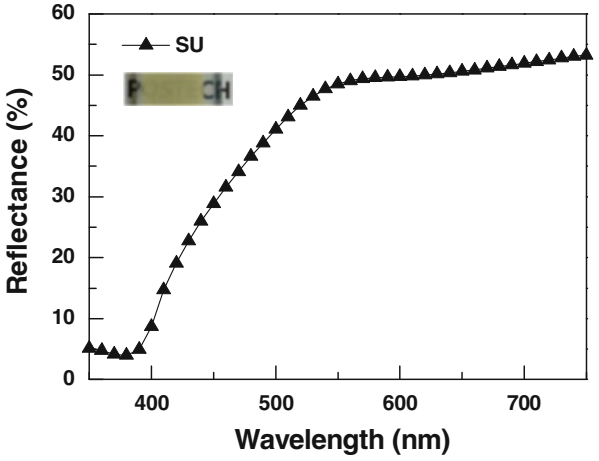

Fig. 2.24 Diffuse reflectance spectra of the SU film. The *inset* is the *top-view* image of the photoanode

Figure 2.26b shows that the recombination time (τ_r) of the SU–NP cell is longer than that of the NP device over the whole light-intensity range. The increased τ_r is attributed to the presence of the relatively defect-free single crystalline TiO_2 nanowires that have far fewer grain boundaries, which may result in the reduced electron trapping phenomena [48, 49]. Additionally, better surface coverage of the QDs at the SU–NP film can promote longer τ_r [42]. This assumption is in agreement

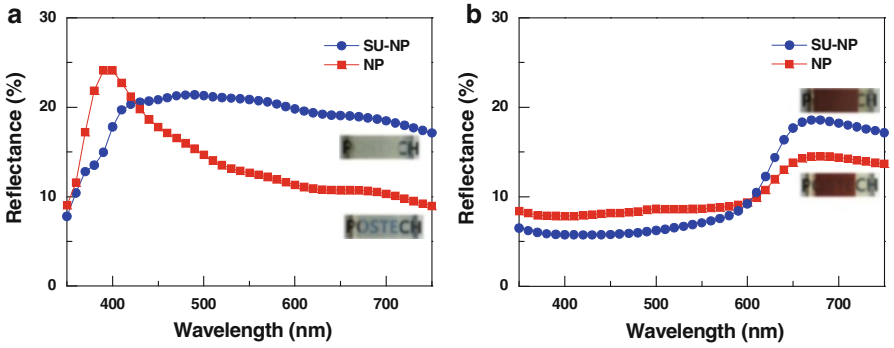

Fig. 2.25 Diffuse reflectance spectra of the SU–NP composite film and the NP film before (**a**) and after (**b**) QDs deposition

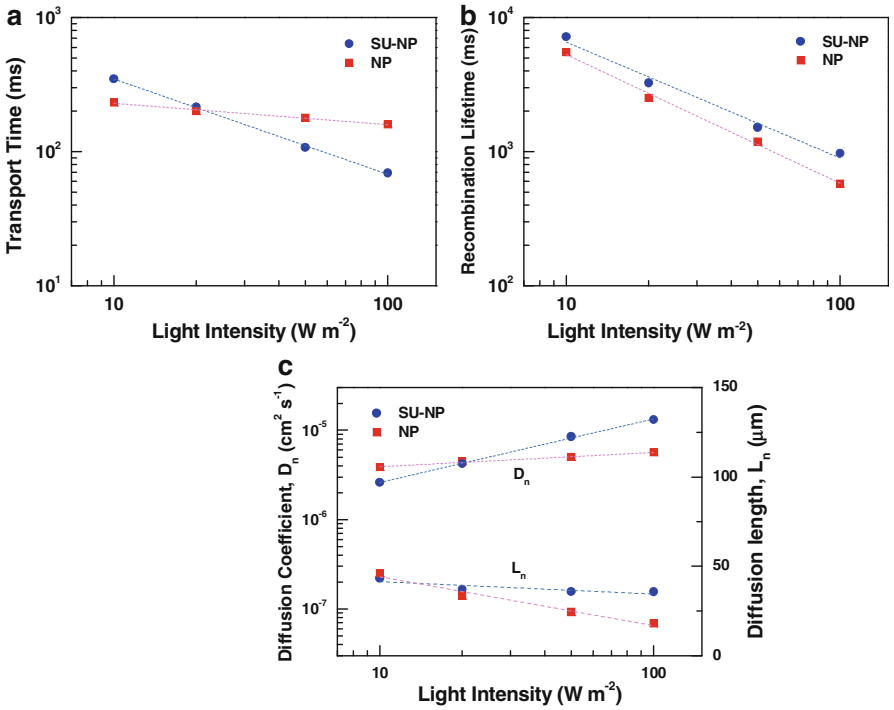

Fig. 2.26 Incident light-intensity-dependent transport time constant (**a**), recombination lifetime (**b**), and electron diffusion coefficient and effective diffusion length (**c**) for the QDSSCs based on the SU–NP composite film and the NP film measured under 625 nm LED illumination

with the previous analysis obtained from the TEM images. As shown in Fig. 2.26c, the effective electron diffusion length (L_n) of the SU–NP cell (35.69 μm) is around twice as thick as that of the NP cell (17.97 μm) under the light intensity of 100 W m^{-2}. On the basis of the increased τ_r, improved photoelectron densities n

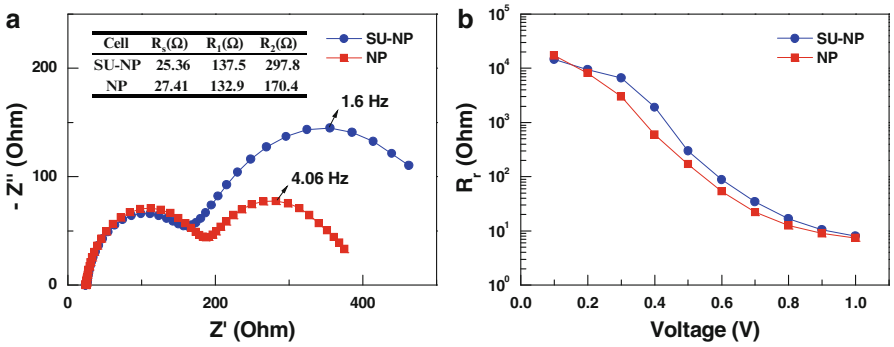

Fig. 2.27 (**a**) Nyquist plots of the EIS spectra and (**b**) R_{ct} for the CdS/CdSe/ZnS QDSSCs with the SU–NP composite and the NP films under dark. The *inset* of (**a**) is corresponding values of fitting parameters

$(n \propto J_{sc}\tau_r)$ [50] yield a higher V_{oc} [51] in the SU–NP cell. Consequently, η_{cc} of the SU–NP cell (92.9 %) was 20.6 % larger than that of the NP device.

Typical Nyquist plots of both cells under dark are presented in Fig. 2.27a. τ_r is estimated to be 625 and 246 ms for the SU–NP and the NP cells, respectively. Figure 2.27b shows R_{ct} for both cells which decreases with increasing applied voltage [40]. It is observed that the SU–NP cell has higher R_{ct} than the NP cell at various applied voltages. This result implies that the recombination is greatly suppressed at the SU TiO_2/polysulphide electrolyte interface, which offers a higher V_{oc}, J_{sc} and improved conversion efficiency. Therefore, it is reasonable to conclude that higher J_{sc} is mainly due to the higher η_{cc}, and partially due to the higher η_{lh} of the SU–NP hybrid composite QDSSCs.

2.5 Conclusions

In recent years, extensive research efforts have been made to implement high-performance QDSSCs. One of the research trends driving innovations is the material engineering of the oxide nanostrucutres for photoanodes. In this article, two representative approaches were introduced in the development of photoelectrodes for QDSSCs: tertiary-hierarchically-structured mesoporous spherical TiO_2 (MS TiO_2) and the sea urchin TiO_2 (SU TiO_2).

The tertiary-hierarchically-structured MS TiO_2 was used as a working electrode for CdS QDSSCs. A conversion efficiency of 1.9 % was achieved with the MS TiO_2, which is 58 % higher than the cells made with conventional nanocrystalline TiO_2 at AM 1.5 one sun illumination. The improved cell performance in the MS TiO_2 cell is attributed to its large surface area, high internal reflectance, and more accessible external pores.

The sea urchin TiO_2 (SU TiO_2) particles composed of rutile TiO_2 nanoneedles and TiO_2 nanoparticles (NP) have been synthesized through a solvothermal process. For the cell fabrication, the SU–NP hybrid composite film was prepared and compared with the NP film. CdS/CdSe/ZnS QDSSCs made of the SU–NP film achieved a noticeable improvement in the power conversion efficiency: 4.2 versus 3.5 % for the reference cell made of the NP film. We attribute this extraordinary result to the higher photocurrent density (J_{sc}) of the SU–NP cell (18.2 mA cm^{-2}), corresponding to about 20 % improvement in comparison with the NP cell. The origin of the enhanced J_{sc} was investigated in terms of two parameters: the light harvesting efficiency (η_{lh}) and the charge-collection efficiency (η_{cc}). The diffuse reflectance spectra and the intensity-modulated photocurrent/photovoltage spectra confirmed that both η_{lh} and η_{cc} were enhanced due to the internal light scattering and more efficient charge collection.

Therefore, it can be concluded that the MS TiO_2 and the SU–NP hybrid composite can be versatile building blocks for the QDSSCs.

Acknowledgments This work is financially supported by Pohang Steel Corporation (POSCO) through Steel Nano-Fusion Program (Project No. 2010Y110) and partly by the World Class University (WCU) program through the National Research Foundation (NRF) of Korea (Grant No. R31-2008-000-10059-0).

References

1. O'Regan, B., Grätzel, M.: A low-cost, high-efficiency solar cell based on dye-sensitized colloidal TiO_2 films. Nature **353**, 737–740 (1991)
2. Yu, W.W., Qu, L., Guo, W., Peng, X.: Experimental determination of the extinction coefficient of CdTe, CdSe, and CdS nanocrystals. Chem. Mater. **15**, 2854–2860 (2003)
3. Nazeeruddin, M.K., Kay, A., Rodicio, I., Humphry-Baker, R., Mueller, E., Liska, P., Vlachopoulos, N., Grätzel, M.: Conversion of light to electricity by cis-X2bis(2,2′-bipyridyl-4,4′-dicarboxylate)ruthenium(II) charge-transfer sensitizers (X = Cl-, Br-, I-, CN-, and SCN-) on nanocrystalline titanium dioxide electrodes. J. Am. Chem. Soc. **115**, 6382–6390 (1993)
4. Nazeeruddin, M.K., Zakeeruddin, S.M., Humphry-Baker, R., Jirousek, M., Liska, P., Vlachopoulos, N., Shklover, V., Fischer, C.-H., Grätzel, M.: Acid-base equilibria of (2,2-′-bipyridyl-4,4′-dicarboxylic acid)ruthenium(II) complexes and the effect of protonation on charge-transfer sensitization of nanocrystalline titania. Inorg. Chem. **38**, 6298–6305 (1999)
5. Gorer, S., Hodes, G.: Quantum size effects in the study of chemical solution deposition mechanisms of semiconductor films. J. Phys. Chem. **98**, 5338–5346 (1994)
6. Nozik, A.J.: Exciton multiplication and relaxation dynamics in quantum dots: applications to ultrahigh-efficiency solar photon conversion. Inorg. Chem. **44**, 6893–6899 (2005)
7. Hanna, M.C., Nozik, A.J.: Solar conversion efficiency of photovoltaic and photoelectrolysis cells with carrier multiplication absorbers. J. Appl. Phys. **100**, 074510 (2006)
8. Chou, T.P., Zhang, Q., Fryxell, G.E., Cao, G.Z.: Hierarchically structured ZnO film for dye-sensitized solar cells with enhanced energy conversion efficiency. Adv. Mater. **19**, 2588–2592 (2007)
9. Koo, H.-J., Kim, Y.J., Lee, Y.H., Lee, W.I., Kim, K., Park, N.-G.: Nano-embossed hollow spherical TiO_2 as bifunctional material for high-efficiency dye-sensitized solar cells. Adv. Mater. **20**, 195–199 (2008)

10. Chen, D., Huang, F., Cheng, Y.-B., Caruso, R.A.: Mesoporous anatase TiO_2 beads with high surface areas and controllable pore sizes: a superior candidate for high-performance dye-sensitized solar cells. Adv. Mater. **21**, 2206–2210 (2009)
11. Park, Y.C., Chang, Y.J., Kum, B.G., Kong, E.H., Son, J.Y., Kwon, Y.S., Park, T., Jang, H.M.: Size-tunable mesoporous spherical TiO_2 as a scattering overlayer in high-performance dye-sensitized solar cells. J. Mater. Chem. **21**, 9582–9586 (2011)
12. Park, Y.C., Kong, E.H., Chang, Y.J., Kum, B.G., Jang, H.M.: Tertiary hierarchically structured TiO_2 for CdS quantum-dot-sensitized solar cells. Electrochim. Acta **56**, 7371–7376 (2011)
13. Efros, A.L., Rosen, M.: The electronic structure of semiconductor nanocrystals. Annu. Rev. Mater. Sci. **30**, 475–521 (2000)
14. Kamat, P.V.: Quantum dot solar cells. Semiconductor nanocrystals as light harvesters. J. Phys. Chem. C **112**, 18737–18753 (2008)
15. Brus, L.E.: A simple model for the ionization potential, electron affinity, and aqueous redox potentials of small semiconductor crystallites. J. Chem. Phys. **79**, 5566–5571 (1983)
16. Kurisu, H., Tanaka, T., Karasawa, T., Komatsu, T.: Pressure induced quantum confined excitons in layered metal tri-iodide crystals. Jpn. J. Appl. Phys. **32**, 285–287 (1993)
17. Lee, C.-J., Mizel, A., Banin, U., Cohen, M.L., Paul Alivisatos, A.: Observation of pressure-induced direct-to-indirect band gap transition in InP nanocrystals. J. Chem. Phys. **113**, 2016–2020 (2000)
18. Nozik, A.J.: Spectroscopy and hot electron relaxation dynamics in semiconductor quantum wells and quantum dots. Annu. Rev. Phys. Chem. **52**, 193–231 (2001)
19. Williams, F., Nozik, A.J.: Irreversibilities in the mechanism of photoelectrolysis. Nature **271**, 137–139 (1978)
20. Boudreaux, D.S., Williams, F., Nozik, A.J.: Hot carrier injection at semiconductor-electrolyte junctions. J. Appl. Phys. **51**, 2158–2163 (1980)
21. Christensen, O.: Quantum efficiency of the internal photoelectric effect in silicon and germanium. J. Appl. Phys. **47**, 689–695 (1976)
22. Wolf, M., Brendel, R., Werner, J.H., Queisser, H.J.: Solar cell efficiency and carrier multiplication in $Si_{1-x}Ge_x$ alloys. J. Appl. Phys. **83**, 4213–4221 (1998)
23. Nozik, A.J.: Quantum dot solar cells. Physica E **14**, 115–120 (2002)
24. Nozik, A.J.: Multiple exciton generation in semiconductor quantum dots. Chem. Phys. Lett. **457**, 3–11 (2008)
25. Klimov, V.I.: Mechanisms for photogeneration and recombination of multiexcitons in semiconductor nanocrystals: implications for lasing and solar Energy. J. Phys. Chem. B **110**, 16827–16845 (2006)
26. Dean, J.A.: Lange's Handbook of Chemistry, 14th edn. McGraw-Hill, New York (1992)
27. Weast, R.C.: Handbook of Chemistry and Physics, 56th edn. CRC, Cleveland (1975)
28. Lee, Y.-L., Chang, C.-H.: Efficient polysulfide electrolyte for CdS quantum dot-sensitized solar cells. J. Power Sources **185**, 584–588 (2008)
29. Bisquert, J., Zaban, A., Greenshtein, M., Mora-Seró, I.: Determination of rate constants for charge transfer and the distribution of semiconductor and electrolyte electronic energy levels in dye-sensitized solar cells by open-circuit photovoltage decay method. J. Am. Chem. Soc. **126**, 13550–13559 (2004)
30. Ondersma, J.W., Hamann, T.W.: Impedance investigation of dye-sensitized solar cells employing outer-sphere redox shuttles. J. Phys. Chem. C **114**, 638–645 (2010)
31. Wang, Q., Ito, S., Grätzel, M., Fabregat-Sañtiago, F., Mora-Seró, I., Bisquert, J., Bessho, T., Imai, H.: Characteristics of high efficiency dye-sensitized solar cells. J. Phys. Chem. B **110**, 25210–25221 (2006)
32. Han, L., Koide, N., Chiba, Y., Mitate, T.: Modeling of an equivalent circuit for dye-sensitized solar cells. Appl. Phys. Lett. **84**, 2433–2435 (2004)
33. Kern, R., Sastrawan, R., Ferber, J., Stangl, R., Luther, J.: Modeling and interpretation of electrical impedance spectra of dye solar cells operated under open-circuit conditions. Electrochim. Acta **47**, 4213–4225 (2002)

34. Schlichthörl, G., Park, N.G., Frank, A.J.: Evaluation of the charge-collection efficiency of dye-sensitized nanocrystalline TiO_2 solar cells. J. Phys. Chem. B **103**, 782–791 (1999)
35. van de Lagemaat, J., Frank, A.J.: Nonthermalized electron transport in dye-sensitized nanocrystalline TiO_2 films: transient photocurrent and random-walk modeling studies. J. Phys. Chem. B **105**, 11194–11205 (2001)
36. Pathan, H.M., Lokhande, C.D.: Deposition of metal chalcogenide thin films by successive ionic layer adsorption and reaction (SILAR) method. Bull. Mater. Sci. **27**, 85–111 (2004)
37. Sudhagar, P., Jung, J.H., Park, S., Sathyamoorthy, R., Ahn, H., Kang, Y.S.: Self-assembled CdS quantum dots-sensitized TiO_2 nanospheroidal solar cells: structural and charge transport analysis. Electrochim. Acta **55**, 113–117 (2009)
38. Chen, J., Li, C., Zhao, D.W., Lei, W., Zhang, Y., Cole, M.T., Sun, X.W., Milne, W.I.: A quantum dot sensitized solar cell based on vertically aligned carbon nanotube templated ZnO arrays. Electrochem. Commun. **12**, 1432–1435 (2010)
39. Lowell, S., Shields, J.E.: Power Surface Area and Porosity. Chapman & Hall, London (1991)
40. Mora-Seró, I., Giménez, S., Fabregat-Sañtiago, F., Gómez, R., Shen, Q., Toyoda, T., Bisquert, J.: Recombination in quantum dot sensitized solar cells. Acc. Chem. Res. **42**, 1848–1857 (2009)
41. Guijarro, N., Lana-Villarreal, T., Mora-Seró, I., Bisquert, J., Gómez, R.: CdSe quantum dot-sensitized TiO_2 electrodes: effect of quantum dot coverage and mode of attachment. J. Phys. Chem. C **113**, 4208–4214 (2009)
42. Kong, E.-H., Chang, Y.-J., Park, Y.-C., Yoon, Y.-H., Park, H.-J., Jang, H.M.: Sea urchin TiO_2-nanoparticle hybrid composite photoelectrodes for CdS/CdSe/ZnS quantum-dot-sensitized solar cells. Phys. Chem. Chem. Phys. **14**, 4620–4625 (2012)
43. Jun, Y.W., Casula, M.F., Sim, J.H., Kim, S.Y., Cheon, J., Alivisatos, A.P.: Surfactant-assisted elimination of a high energy facet as a means of controlling the shapes of TiO_2 nanocrystals. J. Am. Chem. Soc. **125**, 15981–15985 (2003)
44. Peng, X.G., Manna, L., Yang, W.D., Wickham, J., Scher, E., Kadavanich, A., Alivisatos, A.P.: Shape control of CdSe nanocrystals. Nature **404**, 59–61 (2000)
45. Barnard, A.S., Curtiss, L.A.: Prediction of TiO_2 nanoparticle phase and shape transitions controlled by surface chemistry. Nano Lett. **5**, 1261–1266 (2005)
46. Adachi, M., Murata, Y., Takao, J., Jiu, J.T., Sakamoto, M., Wang, F.M.: Highly efficient dye-sensitized solar cells with a titania thin-film electrode composed of a network structure of single-crystal-like TiO_2 nanowires made by the "Oriented Attachment" mechanism. J. Am. Chem. Soc. **126**, 14943–14949 (2004)
47. Zhu, K., Neale, N.R., Miedaner, A., Frank, A.J.: Enhanced charge-collection efficiencies and light scattering in dye-sensitized solar cells using oriented TiO_2 nanotubes arrays. Nano Lett. **7**, 69–74 (2007)
48. Jiu, J.T., Isoda, S., Wang, F.M., Adachi, M.: Dye-sensitized solar cells based on a single-crystalline TiO_2 nanorod film. J. Phys. Chem. B **110**, 2087–2092 (2006)
49. Kang, S.H., Choi, S.H., Kang, M.S., Kim, J.Y., Kim, H.S., Hyeon, T., Sung, Y.E.: Nanorod-based dye-sensitized solar cells with improved charge collection efficiency. Adv. Mater. **20**, 54–58 (2008)
50. Schlichthörl, G., Huang, S.Y., Sprague, J., Frank, A.J.: Band edge movement and recombination kinetics in dye-sensitized nanocrystalline TiO_2 solar cells: a study by intensity modulated photovoltage spectroscopy. J. Phys. Chem. B **101**, 8141–8155 (1997)
51. Frank, A.J., Kopidakis, N., van de Lagemaat, J.: Electrons in nanostructured TiO_2 solar cells: transport, recombination and photovoltaic properties. Coord. Chem. Rev. **248**, 1165–1179 (2004)

http://www.springer.com/978-1-4614-8147-8

Quantum Dot Solar Cells
Wu, J.; Wang, Z.M. (Eds.)
2014, XIV, 387 p. 220 illus., 173 illus. in color.,
Hardcover
ISBN: 978-1-4614-8147-8